Unforced interannual to decadal variability of global radiation imbalance:

Role of low clouds

- 3 Ayumu Miyamoto, a Shang-Ping Xie, a, and Clara Deserb
- ^a Scripps Institution of Oceanography, University of California San Diego, La Jolla, California,
 - USA
- ^b National Center for Atmospheric Research, Boulder, Colorado, USA

Revision submitted to Journal of Climate on October 19, 2025

Corresponding author: Ayumu Miyamoto, aymiyamoto@ucsd.edu

ABSTRACT: The global radiation imbalance at the top of the atmosphere (TOA) is an important indicator of the climate response to anthropogenic greenhouse forcing. Natural variability perturbs this radiation imbalance on interannual and decadal timescales, confounding the externally forced 10 signal. However, limited observations hinder the effort to understand the mechanisms for internally generated radiation imbalance. This study investigates the natural variability of global TOA 12 radiation using a 500-year preindustrial coupled simulation with the Community Earth System 13 Model version 2, and a corresponding atmospheric model simulation forced with daily sea surface temperature (SST) and sea ice from the coupled run. Variations in global TOA radiation lead those in tropical Pacific SST and global-mean surface temperature by 90° in phase. The analysis 16 reveals the dominant role of low-cloud radiative effects with timescale-dependent spatial patterns. 17 On interannual timescales, low cloud anomalies are distributed across tropical and extratropical 18 oceans, with maxima over the equatorial northeast Pacific. In contrast, decadal variability of global 19 TOA radiation is due to variations of eastern subtropical low cloud decks, coupled with underlying 20 SST anomalies. These low cloud-SST co-variations are triggered by stochastic extratropical atmospheric variability. This timescale dependence likely reflects the characteristics of these 22 drivers: the amplitude of El Niño-Southern Oscillation peaks at interannual timescales due to 23 tropical ocean dynamics, whereas extratropical stochastic forcing becomes increasingly important on decadal and longer timescales. Recent satellite observations of TOA radiation corroborate both 25 mechanisms. This study underscores the importance of subtropical low cloud-SST co-variations 26 induced by extratropical atmospheric forcing in unforced variability of global energy imbalance.

28 1. Introduction

The Earth's energy budget is a fundamental physical property of the climate system, and governs
the rise in global-mean surface temperature due to greenhouse gas forcing. The climate system
responds to radiative forcing (F) at the top of the atmosphere (TOA) by modifying longwave
emission and incoming solar radiation via changes in surface temperature. This global-mean
energy budget may be cast as

$$N = F + \lambda T \tag{1}$$

where N is the net radiation (hereafter expressed as GMTOA; positive value for downward flux) and λ the climate feedback parameter which characterizes radiative feedback from perturbation of global-mean surface temperature (GMST) T (Gregory et al. 2004). Reducing uncertainty in projections of global warming is a pressing task for the climate research community. Radiative feedback estimates from historical changes (N-F)/T have been extensively investigated to improve our understanding of and constraints on future warming (Sherwood et al. 2020).

In this context, decadal changes in GMTOA garner considerable attention. Satellite observations from Clouds and the Earth's Radiant Energy System (CERES) have yielded a continuous record of GMTOA for more than two decades (Loeb et al. 2024). The data record features a striking positive trend in planetary energy uptake, exceeding that simulated by global climate models (Raghuraman et al 2021; Olonscheck and Rugenstein 2023). GMTOA and associated radiative feedbacks in the historical period are often estimated using atmospheric general circulation models (AGCMs) forced with observed sea surface temperature (SST) and sea ice, i.e., the AMIP (Atmospheric Model Intercomparison Project) protocol. The model simulations revealed substantial decadal variations in radiative feedbacks (Gregory and Andrews 2016; Andrews et al. 2018).

In addition to anthropogenic radiative forcing (e.g., CO₂, aerosols), natural variability needs to be considered in the historical variations of GMTOA (Dessler et al. 2018; Wills et al. 2021). For natural variability, the relationship between GMTOA and GMST is complex and distinct from the forced response. Their concurrent correlation is nearly zero, and the peak correlation occurs with GMTOA leading by 90°, such that planetary heat uptake acts to raise GMST (Xie et al. 2016). The peak lagged correlation is modest on decadal timescales, implying the GMTOA variations only loosely related to GMST.

This raises an important question: what causes natural decadal GMTOA variations? In quadrature 56 with each other (Xie et al. 2016), GMST is unlikely the major driver for GMTOA in natural 57 variability. Instead, we hypothesize that subtropical low clouds play an important role in the GMTOA variations. While tropical Pacific SST changes modulate subtropical low clouds through deep convective adjustment (Zhou et al. 2016), extratropical atmospheric variability and resultant 60 eastern subtropical SST anomalies can locally drive the low cloud variations (Larson et al. 2024; 61 Miyamoto and Xie 2025). Previous studies highlighted the tropical Pacific SST effect in relation to radiatively forced warming patterns—known as the pattern effect (e.g., Senior and Mitchell 2000; Dong et al. 2020; Andrews et al. 2022), but the subtropical SST effect has not been extensively examined. The present study investigates unforced interannual to decadal variability of GMTOA based on 66 a 500-year simulation under constant preindustrial radiative forcing with a state-of-the-art global 67 climate model, Community Earth System Model version 2 (CESM2; Danabasoglu et al. 2020), 68 and a corresponding "perfect-model" AMIP simulation forced with daily SST and sea ice from the coupled run. Unlike previous studies that examined GMTOA variations associated with GMST or 70 selected SST modes (e.g., Xie et al. 2016; Wills et al. 2021), this study focuses on GMTOA itself 71 without making any a priori assumptions about a relationship with SST modes. Our GMTOAcentric analysis reveals the regions and radiative components (cloud and clear-sky contributions) 73 that are crucial in unforced GMTOA variability. The perfect AMIP run is utilized to disentangle 74 stochastic atmospheric forcing and SST effects on the GMTOA variations. A comparison of

The rest of the paper is organized as follows. Section 2 describes the data used in this study.

Sections 3 and 4 document the natural GMTOA variability in CESM2 on interannual and decadal timescales, respectively. Section 5 compares with the recent CERES observations and discusses the timescale dependence. Section 6 concludes the paper with a summary of the key findings.

interannual and decadal GMTOA variations aids the interpretation of the short CERES record.

81 **2. Data**

82 a. Preindustrial simulations

We use a 500-year fully coupled CESM2 simulation with constant 1850-level radiative forcing (Danabasoglu et al. 2020; hereafter labeled CESM). Its atmosphere and ocean resolutions are

- nominally 1° in the horizontal with increasing meridional ocean resolution toward the equator.
- ₈₆ CESM2 simulates natural variability such as El Niño-Southern Oscillation (ENSO) and tropical
- Pacific decadal variability (TPDV) (Danabasoglu et al. 2020; Capotondi et al. 2020). The model
- also reproduces subtropical low clouds off the west coasts of continents (Fig. 1) and their positive
- feedback with underlying SST (Kang et al. 2023; Larson et al. 2024; Miyamoto and Xie 2025).
- In parallel with the coupled run, a single-member AMIP simulation with identical boundary
- conditions (hereafter labeled CAM) was conducted by the CESM2 Climate Variability and Change
- Working Group (CVCWG). In this setup, the atmospheric component of CESM2, the Community
- Atmosphere Model version 6 (CAM6), is forced with daily SST and sea ice from CESM. This
- perfect-model/SST framework allows for a direct comparison with CESM (in a statistical sense
- owing to the limited ensemble size). If CAM fails to reproduce an anomaly of cloud, temperature,
- and wind in CESM, the anomaly can be attributed to stochastic atmospheric variability.

97 b. Observational data

For observational datasets, we use the Optimum Interpolation Sea Surface Temperature (OISST) version 2 (Huang et al. 2021) for SST, the CERES Energy Balanced and Filled edition 4.2 (Loeb et al. 2018) for radiative fluxes, the Moderate Resolution Imaging Spectroradiometer (MODIS) onboard Terra collection 6.1 (Platnick et al. 2003) for cloud cover, and the ERA5 global atmospheric reanalysis (Hersbach et al. 2020) for other meteorological variables. The horizontal resolution of the datasets is 0.25° for OISST and 1° for the others. For the MODIS low cloud cover, the random overlap assumption is applied to suppress the shielding effect of high clouds, as in Miyamoto and Xie (2025).

106 c. AMIP simulations with observed SST

In parallel with the CERES observations, we analyze two versions of AMIP simulations prescribed with observed SST and sea ice; one conducted by CVCWG uses CAM6 and the other
uses the Geophysical Fluid Dynamics Laboratory Atmospheric Model version 4 (AM4; Zhao et al.
2018). Hereafter, we refer to them as CAMobs and AMobs, respectively. The resolution of AM4 is
approximately 100 km with 33 levels in the vertical. CAMobs covers the period 1880-2021, while
AM4obs covers 1982-2021. Both models are radiatively forced by historical forcing up to 2014

and Shared Socioeconomic Pathway scenarios (SSP3-7.0 for CAMobs and SSP2-4.5 for AMobs)
from the Coupled Model Intercomparison Project phase 6 (Eyring et al. 2016). CAMobs uses the
monthly-mean SST and sea ice from Extended Reconstructed SST version 5 (Huang et al. 2017)
and OISST version 2, respectively, whereas AMobs uses daily-mean OISST version 2 for both
SST and sea ice. Both models have 10 ensemble members each, and their ensemble averages are
analyzed.

d. Preprocessing

All data are interpolated onto a 2.5° grid, linearly detrended, and smoothed with a 12-month running mean. To decompose the anomalies into interannual and decadal components, a Lanczos filter with a cutoff period of 10 years was applied to the 500-year CESM and CAM simulations. For the decadal components, only calendar-year (January-to-December) 12-month averages are analyzed. The observational data and AMIP simulations are analyzed over the period from 2001 to 2021. The Lanczos time filtering was not applied because of the short observational record.

e. Statistical test

We assess the statistical significance of correlation and regression coefficients using a Student's t-test. To estimate the effective sample size, we calculate effective decorrelation time T_e following Metz (1991):

$$T_e = 1 + 2\sum_{\tau=1}^{L} \left(1 - \frac{\tau}{L}\right) R_{XX}(\tau) R_{YY}(\tau). \tag{2}$$

 $R_{XX}(\tau)$ and $R_{YY}(\tau)$ denote autocorrelation functions of variables X and Y at a lag of τ months/years.

L is set to 120 months for interannual anomalies and 50 years for decadal anomalies. The effective sample size N_e is then given by

$$N_e = \frac{N_t}{T_e} \tag{3}$$

where N_t is the number of samples.

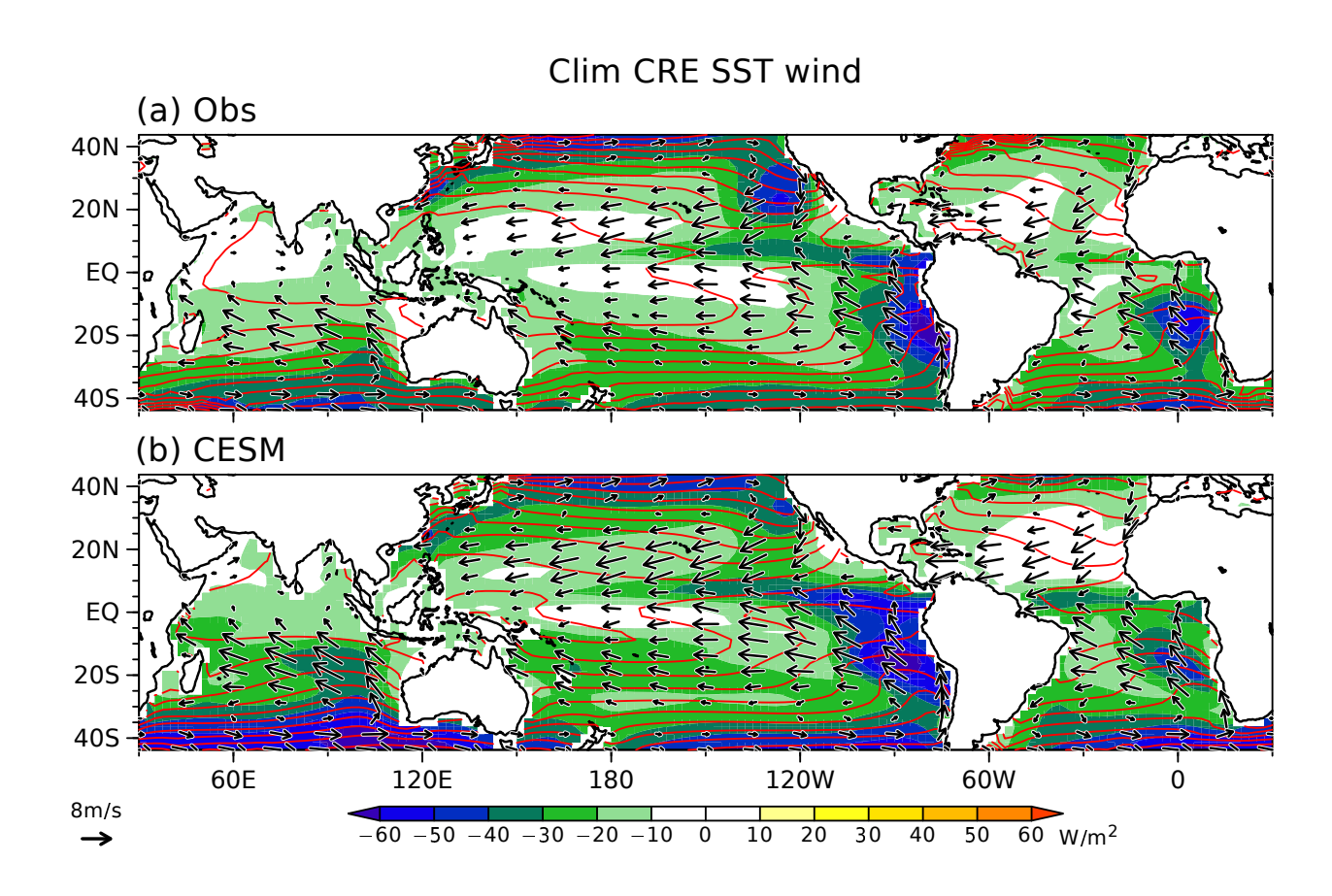


Fig. 1. Annual-mean climatology of SST (contoured for every 2 $^{\circ}$ C), surface wind (arrows; m s⁻¹), and TOA cloud radiative effect (CRE; shading; W m⁻²; positive values for heating) from (a) observations and (b) CESM.

3. Interannual variation

a. Lead-lag relationship

The correlation analysis indicates that GMTOA and GMST are in quadrature for both interannual and decadal variability in CESM (Fig. 2, top two rows). The rise of GMST at a peak radiative energy input is consistent with unforced variations in observations and other climate models (Xie et al. 2016; Lutsko and Takahashi 2018; Proistosescu et al. 2018). The GMTOA is highly correlated with the global net surface heat flux (Fig. S1), with the ocean absorbing 82% and 92% of the radiative energy input at lag 0 for interannual and decadal variability, respectively. The lagged relationship with GMST contrasts with forced climate change where radiative feedback is assumed to be proportional to GMST as in Eq. (1).

For interannual variability, the GMTOA is dominated by and closely tracks cloud radiative effect (CRE; Fig. 2h), while the upward clear-sky flux is nearly in phase with GMST (Fig. 2i). At the GMTOA peak, CRE, particularly its shortwave component, accounts for approximately 75%, with a secondary contribution from longwave clear-sky flux (Table 1). The weak concurrent anomalies in GMST and clear-sky fluxes suggest that natural GMTOA variability is not primarily driven by longwave damping on temperature variability (the Planck response or lapse rate feedback). This study therefore focuses on the cloud processes that create GMTOA anomalies under weak GMST anomalies.

Coupled ocean-atmosphere variability and atmospheric stochastic forcing can dictate unforced GMTOA variability (Xie et al. 2016; Lutsko and Takahashi 2018; Proistosescu et al. 2018). Red lines in Figs. 2f-i indicate lag correlation of GMTOA between CESM and CAM, which assesses the SST effect on GMTOA and its lagged relationship in CESM. The autocorrelation of GMTOA in CESM is captured by CAM without significant lead-lag asymmetry (Fig. 2f). Reflecting the ability of CAM to capture the evolution of both CRE and clear-sky flux (Figs. 2h,i), the interannual correlation of GMTOA at lag 0 amounts to 0.71. Noting that single-member CAM has stochastic atmospheric noise unlike the ensemble-mean, this indicates that the ocean effect explains at least half of the CESM GMTOA variations. The strong ocean effect under weak GMST anomalies indicates the importance of SST pattern.

TABLE 1. Global-mean TOA radiative flux (W m⁻²) regressed onto GMTOA from CESM decadal, interannual, and CERES anomalies (left to right). In CESM decadal anomalies, values in parentheses indicate a +1-year lagged anomaly. SW and LW signify shortwave and longwave components, respectively. CLR denotes clear-sky flux. Boldface indicates statistical significance at the 90% confidence level.

	CESM decadal	CESM interannual	CERES
GMTOA	0.12 (0.11)	0.40	0.26
Net CRE	0.09 (0.11)	0.29	0.19
SW CRE	0.09 (0.11)	0.26	0.16
LW CRE	0.00 (0.00)	0.04	0.02
Net CLR	0.02 (0.00)	0.11	0.07
SW CLR	0.00 (0.01)	0.03	-0.02
LW CLR	0.02 (-0.01)	0.08	0.09

172 b. Spatial pattern

Figure 3 shows the time evolution of interannual radiation and surface temperature anomalies 173 regressed onto GMTOA in CESM. At the GMTOA peak, positive net TOA anomalies are distributed 174 across the tropics and part of the extratropical oceans (Fig. 3c). The strongest signal appears in the equatorial eastern Pacific with a secondary maximum in the Southeast Pacific. Over the Pacific, 176 SST anomalies at lag 0 do not resemble any well-known SST modes of variability (Fig. 3d), but 177 the lead-lag regression implies the effect of ENSO. In particular, the GMTOA peak is preceded by a La Niña signature (Fig. 3b) and followed by an El Niño pattern (Fig. 3f), consistent with 179 previous studies (e.g., Lutsko and Takahashi 2018; Wills et al. 2021; Tsuchida et al. 2023). This 180 link with the ENSO transition is confirmed by the high correlation (~ 0.7) between GMTOA and 181 Niño-3.4 SST (5°S-5°N, 170°W-120°W) at lag ±9 months (Fig. 2j). At these lags, GMST is near 182 its peak (Fig. 2g) consistent with the ENSO pacemaker effect on GMST (Kosaka and Xie 2013), 183 while GMTOA is almost zero (Fig. 2f) due to offsetting anomalies over the Pacific and Indian 184 Ocean (Figs. 3a,e).

191 c. Mechanism

The dominance of shortwave CRE in the GMTOA variations implies that low-level clouds play a crucial role through their albedo effect (Klein and Hartmann 1993). Figure 4 shows anomalies in low cloud cover and environmental controlling factors associated with interannual GMTOA

variations in CESM and CAM. Negative anomalies in low cloud cover are distributed across the tropical and extratropical oceans, leading to the increased shortwave energy uptake (Fig. 4a). This low-cloud decrease explains the TOA radiation changes well, with a pattern correlation of -0.83 between low cloud cover and net TOA radiation.

The decrease in low clouds across the tropics is accompanied by the weakening of lower tropo-199 spheric stability measured by Estimated Inversion Strength (EIS; Wood and Bretherton 2006) (Fig. 200 4c). This is partly due to zonally uniform tropical tropospheric cooling (Fig. 4g), a mechanism 201 often invoked in previous literature on pattern effect (Zhou et al. 2016; Fueglistaler 2019; Ceppi 202 and Fueglistaler 2021). The pan-tropical tropospheric temperature follows the moist adiabat set 203 by SST in tropical ascent regions (Sobel et al. 2001). Consistently, negative SST anomalies are 204 distributed in the tropical Indo-Pacific and western Atlantic (Fig. 4i), which persist after a La Niña 205 (Figs. 3b,d,f,h; Enfield and Mayer 1997; Xie et al. 2009). As measured by the SST# index (the 206 temperature of the warmest 30% minus the tropical average SST; Fueglistaler 2019), concurrent 207 SST anomalies over the tropical ascent regions are positively correlated with interannual GMTOA variations (r = 0.52; Fig. S2). Additionally, the pan-tropical cooling may induce a subsidiary 209 positive effect on GMTOA through a reduction in clear-sky outgoing longwave emission (Fig. S3; 210 Andrews and Webb 2018; Ceppi and Fueglistaler 2021).

We emphasize, however, that the spatial pattern of low cloud and EIS anomalies does not align with a simple picture of the free-tropospheric warming effect on the eastern subtropical low cloud decks (e.g., Zhou et al. 2016). For instance, there are weak increases in low clouds off the Californian coast and strong decreases over the western-to-central extratropical Pacific (Fig. 4a). This discrepancy is attributed to SST anomalies and resultant local stability changes (Figs. 4c,i). The North Pacific SST anomalies are likely due to the lingering effect of the Aleutian low weakening caused by the preceding La Niña (Fig. 3b; Alexander et al. 2002; Yang et al. 2023).

The TOA radiation anomalies also peak over the equatorial eastern Pacific, accounting for 23% of GMTOA (black box in Figs. 3c and 5b; 5% of Earth's surface). As shown in the magnified figure, the low cloud decrease peaks not along the equator but slightly to its north (Fig. 5b). Climatologically, the northward flow toward the intertropical convergence zone crosses a sharp SST gradient on the northern flank of the equatorial cold tongue, promoting stratus and shallow cumulus clouds there (Fig. 5a; Deser and Wallace 1990; Small et al. 2005). Consistent with this

climatological-mean state, the changes of equatorial low clouds are attendant with the emergence of warmer cold tongue (Fig. 5e) in the developing El Niño (Fig. 3). This leads to anomalous warm-air advection to the north of the equator, which corresponds well with the decrease in low clouds (Fig. 5d). Thus, developing El Niño plays a crucial role, in addition to decaying La Niña discussed in the previous paragraphs. Similar SST and radiation patterns appear in the regression analysis against Niño-3.4 SST (Fig. S4).

In Fig. 4, corresponding anomalies in CAM are juxtaposed with the CESM results to examine the SST effect. CAM well reproduces the CESM pattern of low cloud anomalies despite its complexity (Fig. 4b). Combined with prescribed SST and simulated tropospheric temperature (Fig. 4h), CAM accurately captures the EIS anomalies (Fig. 4d). The anomalous warm advection due to warm SST anomalies in the eastern equatorial Pacific is also reproduced (Fig. 4f). These results corroborate the effect of ENSO-related SST anomalies on low clouds and therefore GMTOA.

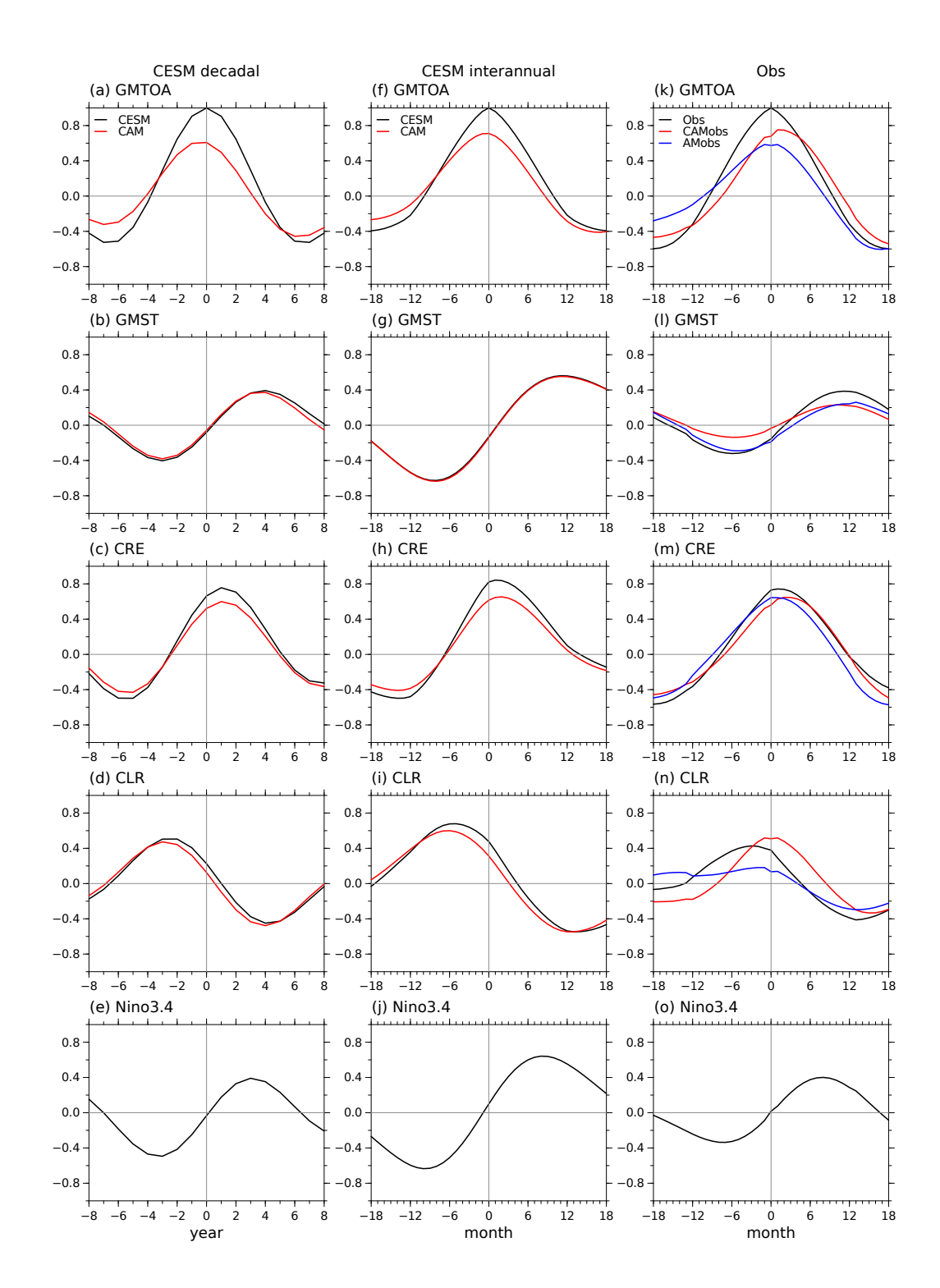


Fig. 2. Lead-lag correlation with GMTOA (positive values for heating) from (a-e) CESM decadal, (f-j) CESM interannual, and (k-o) observed anomalies (black lines). Colored lines denote the correlation of AMIP runs with CESM/CERES GMTOA. (a,f,k) GMTOA, (b,g,l) GMST, (c,h,m) global-mean CRE, (d,i,n) global-mean clear-sky flux, and (e,j,o) Niño-3.4 SST. Note that a positive lag means CESM/CERES GMTOA leads.

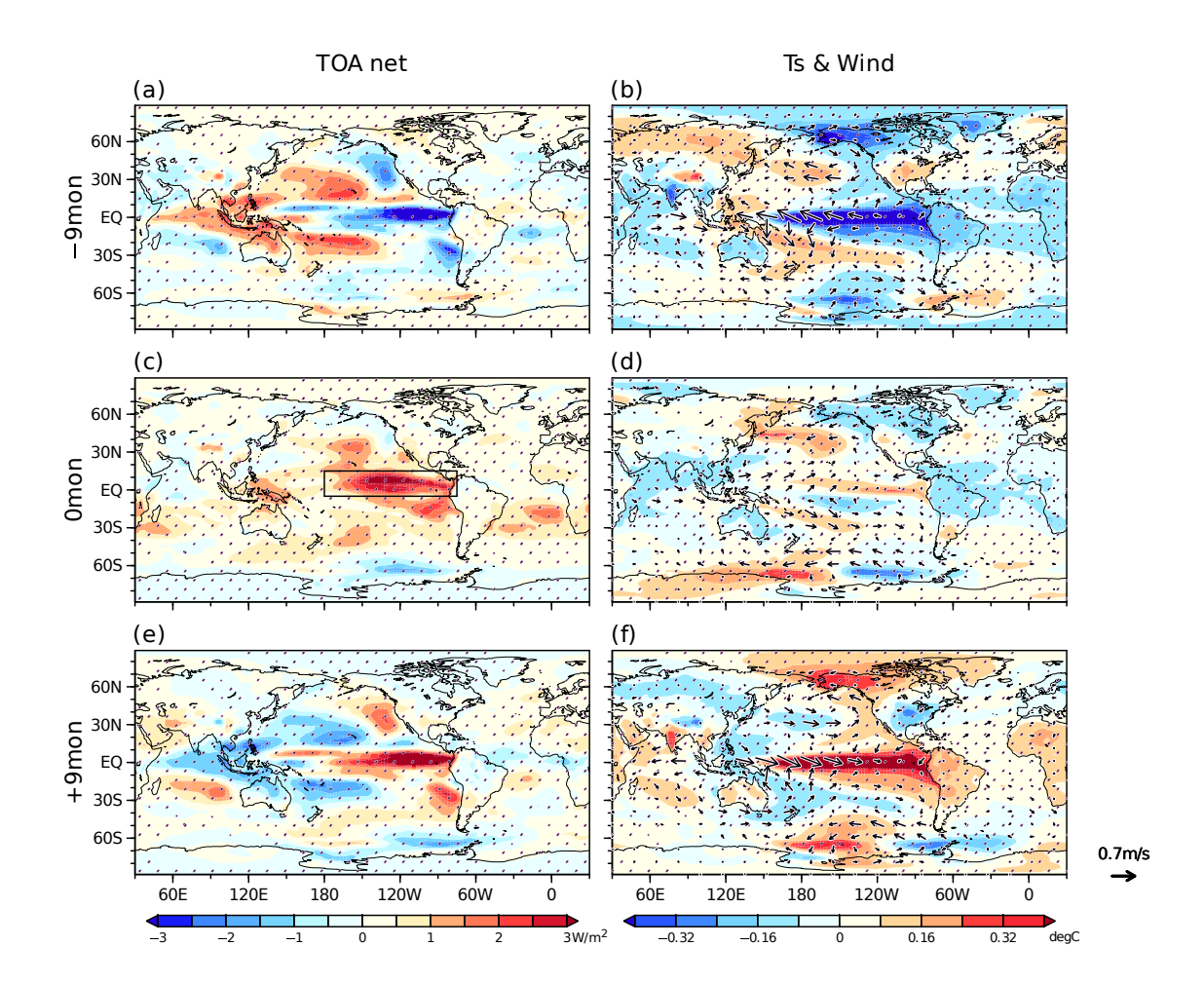


Fig. 3. Spatial pattern and time evolution of interannual GMTOA anomalies in CESM. Lagged regression maps of (a,c,e) TOA radiation (W m⁻²), (b,d,f) surface temperature (shading; °C) and wind (arrows; m s⁻¹; only points with the 90% confidence are drawn) onto CESM interannual GMTOA anomalies at lags (a,b) –9, (c,d) 0, and (e,f) +9 months. Stippling indicates the 90% confidence. Lag-0 TOA radiation anomalies within black box explain 23% of GMTOA.

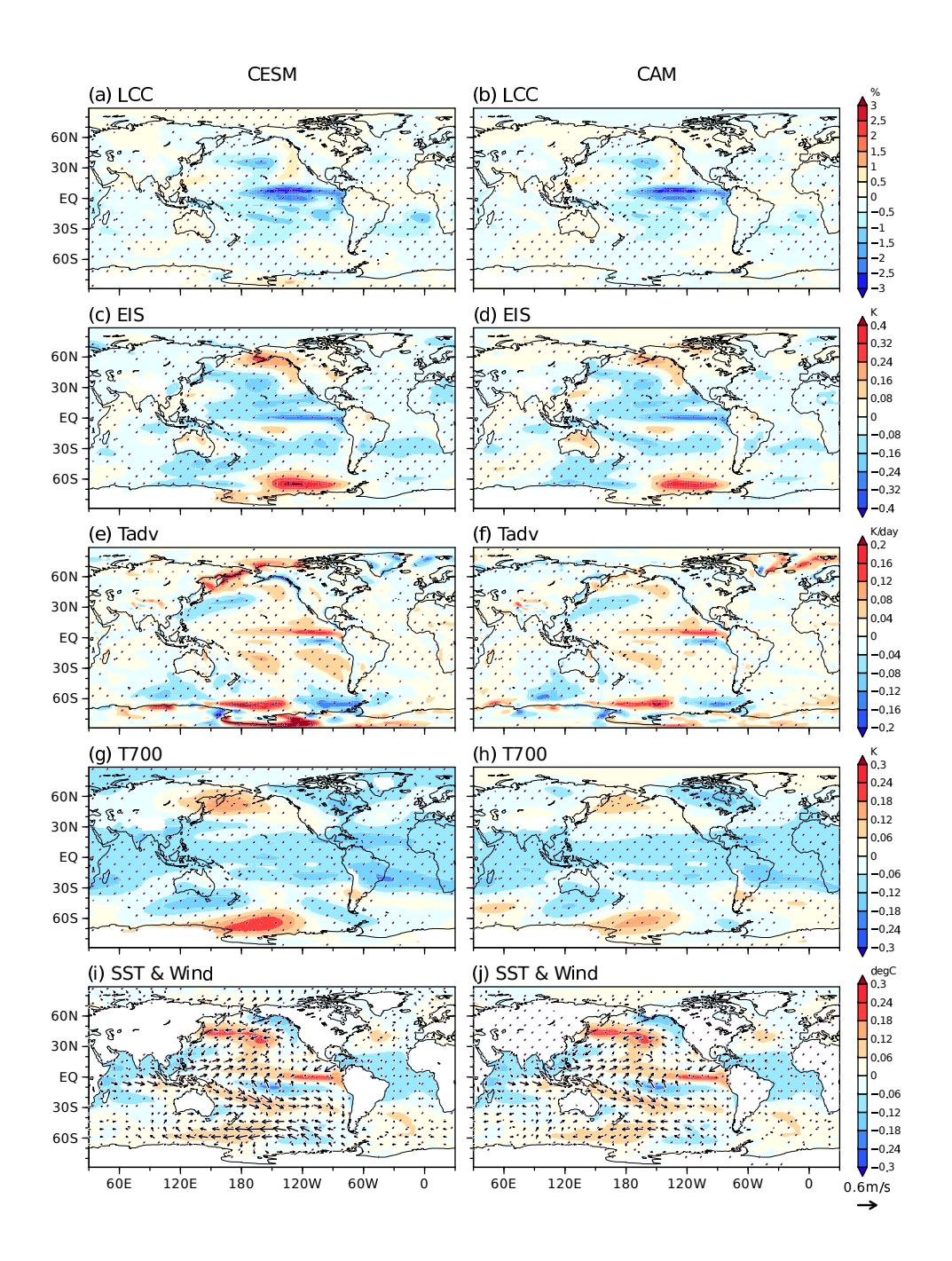


Fig. 4. Regression maps of (a,c,e,g,i) CESM and (b,d,f,h,j) CAM anomalies onto CESM interannual GMTOA at lag 0. (a,b) Low cloud cover (%). (c,d) EIS (K). (e,f) surface temperature advection $(K \ day^{-1})$. (g,h) 700-hPa temperature (K). (i,j) SST (shading; °C) and surface wind (arrows; m s⁻¹; only points with the 90% confidence are drawn). Stippling indicates the 90% confidence.

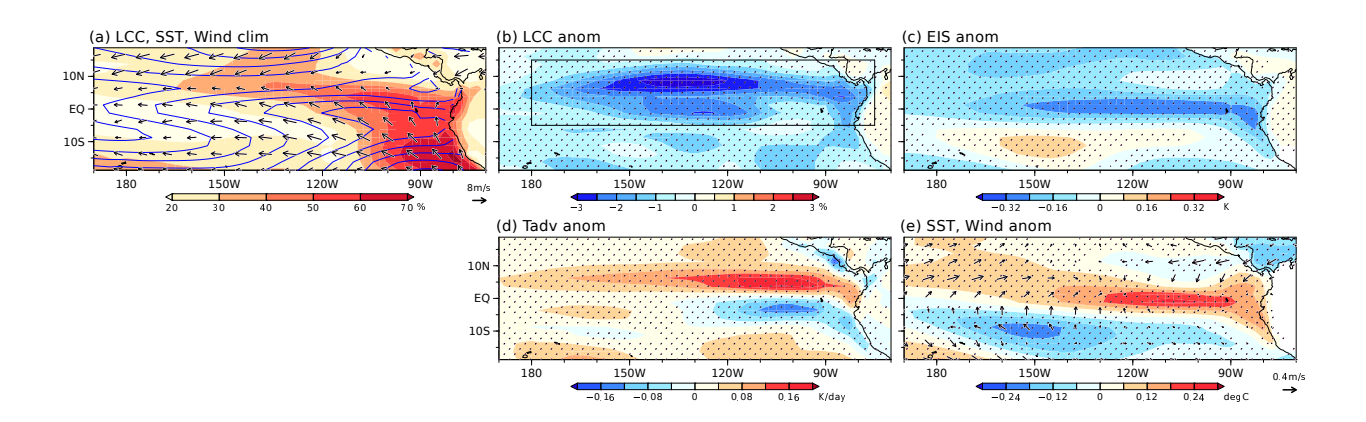


Fig. 5. (a) CESM climatology of low cloud cover (shading; %), SST (contoured for every 1 °C), and surface winds (arrows, m s⁻¹). (b-d) magnified maps of Figs. 4a,c,e,i, respectively. Black box in (b) is the same as in Fig. 3c.

4. Decadal variation

This section investigates the decadal GMTOA variability in CESM and contrasts it with the 245 interannual counterpart. The lead-lag relationships on decadal timescales shown in Fig. 2a-d resemble those on interannual timescales. There is an approximately 90° phase-lagged relationship 247 with GMST (black lines in Figs. 2a,b; Xie et al. 2016), with a weaker peak correlation compared 248 to the interannual correlation. CRE accounts for 75% of the GMTOA peak through shortwave heating, compounded by a secondary clear-sky effect (Table 1). The peak in CRE emerges one year 250 later (Fig. 2c), explaining nearly all the GMTOA anomaly (Table 1). As shown by the red lines 251 in Figs. 2a-d, CAM reasonably captures these features, with a GMTOA correlation coefficient of 0.61 at lag 0 between CESM and CAM. While stochastic atmospheric variability is nonnegligible, this result underpins the quantitative importance of the ocean effect, with the SST pattern playing 254 a key role under weak concurrent GMST anomalies. 255

256 a. Spatial pattern

Figure 6 shows the time evolution of radiation and surface temperature anomalies associated 257 with the decadal GMTOA variations. Despite the similar temporal relationships on interannual and 258 decadal timescales, there are marked differences in the spatial patterns of radiation. Remarkably, peak GMTOA on decadal timescales is associated with marked TOA radiation anomalies in the 260 subtropical low-cloud regions (Figs. 6e,f). Strong positive signals occur over the Northeast Pacific 261 and Southeast Indian Ocean, with a weaker signal over the South Atlantic. A positive signal in the eastern equatorial Pacific is much less dominant than on interannual timescales. The Southeast 263 Pacific signal is not prominent at lag 0 but intensifies rapidly at lag +1, reaching a magnitude 264 comparable to that in the North Pacific and Indian Ocean (Fig. 6g). These strong positive anomalies in the subtropical low cloud regions align with the peak of global-mean CRE (Fig. 2c). 266 The corresponding SST anomalies at lag 0 and +1 years are also localized to the eastern subtropical 267 oceans (Figs. 6f,h), in contrast to the interannual anomalies. Such timescale dependence implies 268 marked differences in the physical processes.

It is noteworthy that the TPDV-like equatorial Pacific SST pattern transitions from a negative to a positive phase across lag 0 (Figs. 6b,j), although the maximum correlation between GMTOA and Niño-3.4 SST drops to 0.4 (Fig. 2e). At lag ±3 year when the TPDV-like SST signals are

maximized, strong radiation changes over the Pacific tend to cancel out (Figs. 6a,i), as in the peak phase of ENSO (Figs. 6a,e). This spatial compensation in TOA radiation associated with 274 decadal fluctuations seems somewhat at odds with previous work claiming the equatorial Pacific 275 warming pattern on global radiation (Zhou et al. 2016; Andrews and Webb 2018). This difference may reflect distinct global energy budgets governing natural variability and forced response. For 277 example, unforced SST fluctuations in the warm pool region, which efficiently induce GMTOA 278 anomalies (Zhou et al. 2017), tend to be small. Indeed, decadal GMTOA variations show a very weak concurrent correlation with the SST# index, in contrast to the interannual variations (Fig. 280 S2). 281

b. Mechanism

300

Figure 7 shows anomalies in low cloud cover and environmental factors associated with decadal 283 GMTOA variations in CESM and CAM. Here, lag +1-year fields are discussed to capture the rapid 284 emergence of the Southeast Pacific signal and associated peak in global-mean CRE. Otherwise, 285 the low-cloud signal is qualitatively the same as the lag-0 fields (Fig. S5). With a high spatial 286 correlation of 0.88, the net radiation anomalies at lag +1 are well explained by anomalous low 287 cloud decrease maximized over over the Northeast Pacific, Southeast Pacific, and South Indian Ocean (Fig. 7a). The low cloud decrease is collocated with weakening of EIS (Fig. 7c). Although 289 free-tropospheric cooling associated with decaying TPDV contributes to the low cloud decrease at 290 lags –1 and 0 (Figs. S5,6), this signal is not obvious at lag 1 (Fig. 7g). Local SST warming strongly controls the decadal decrease of EIS and thus low clouds as positive low cloud-SST feedback (Fig. 292 7i). The low cloud-SST feedback through EIS corroborates CAM's reproducibility of the low 293 cloud changes in CESM (Figs. 7b,d) and consequently GMTOA changes. The weakly opposing 294 signal in the tropical Northeast Atlantic may be due to the lack of a pronounced low cloud deck 295 there (Fig. 1). Similar to yet less dominant than the interannual variations, the decadal decrease in 296 equatorial Pacific low clouds corresponds to the emergence of warm-phase TPDV (Figs. 7a,i). 297 The positive SST anomalies over the eastern subtropical oceans are concurrently associated with poleward wind anomalies extending westward and equatorward (Fig. 7i). These weakened trade 299 wind anomalies induce warm-air advection (Fig. 7e), suppressing turbulent heat loss from the

ocean that, together with radiative heating due to the low cloud decrease, raises the SST (Table

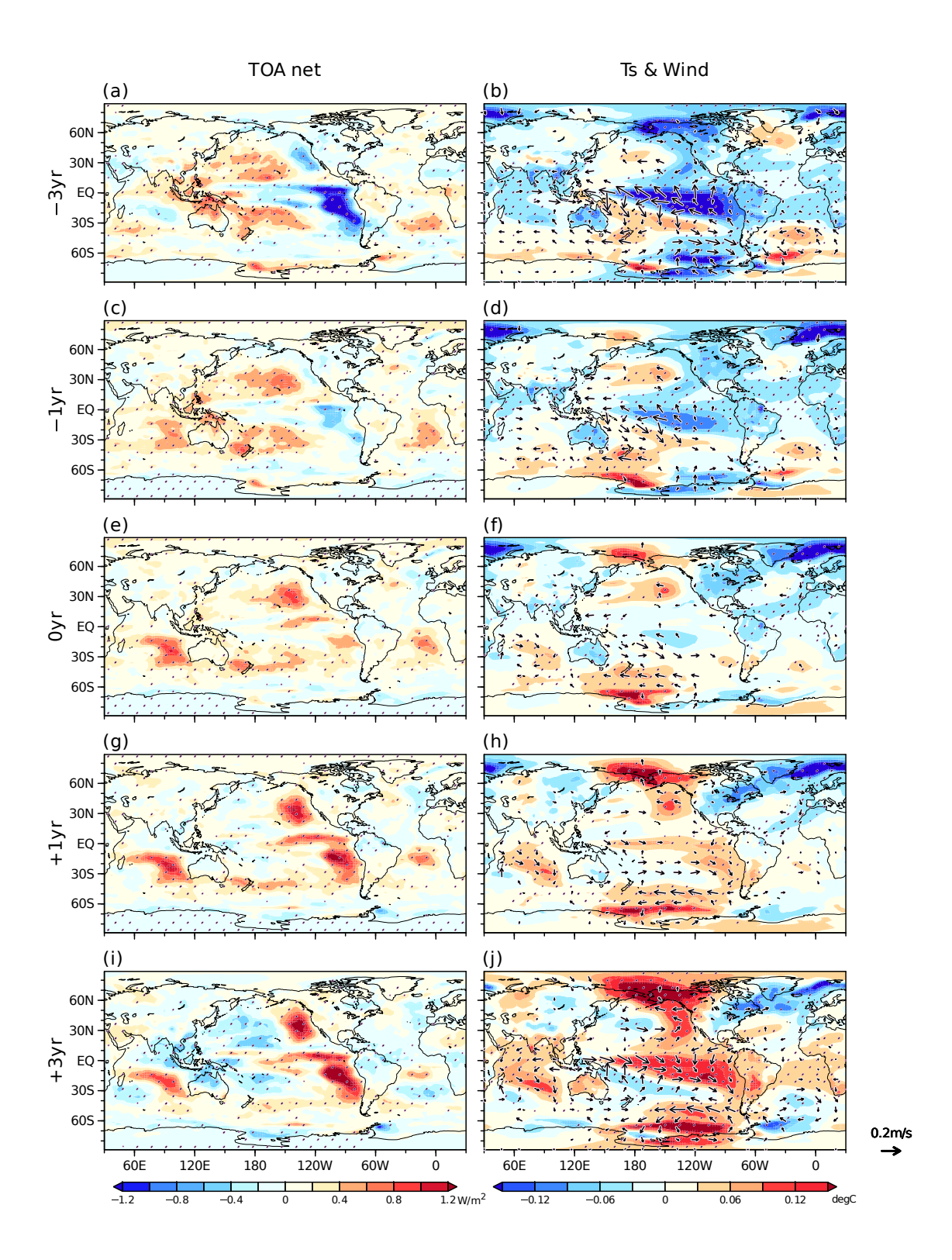


Fig. 6. As in Fig. 3, but for decadal anomalies. Lags (a,b) - 3, (c,d) - 1, (e,f) 0, (g,h) + 1, (i,j) + 3 years.

2). The equatorward extension of these SST anomalies accompanied by anomalous trade winds resembles the meridional modes (Chiang and Vimont 2004; Zhang et al. 2014) generated through wind-evaporation-SST (WES) feedback (Xie and Philander 1994). Modeling studies demonstrated that subtropical low cloud-SST feedback energizes the meridional mode-like variability as joint low cloud-WES feedback (Evan et al. 2013; Bellomo et al. 2014; Miyamoto et al. 2021; Kim et al. 2022; Miyamoto et al. 2023).

The comparison of the wind anomalies between CESM and CAM reveals the origin of the low 308 cloud and meridional mode-like variability. In CESM, the poleward wind anomalies responsible 309 for the elevated SSTs are embedded with extratropical circulation anomalies (Fig. 7i). While CAM 310 partly captures the weakening of trade winds in WES feedback, it underestimates or even fails to 311 simulate these extratropical circulations, except for the modest anomalies over the South Atlantic 312 (Fig. 7j). Additionally, the underestimation of warm-air advection, which acts to decrease low 313 cloud cover directly (Klein et al. 1995; Miyamoto et al. 2018), may contribute to the slightly 314 underestimated low cloud anomalies in CAM (Figs. 7b,f). In the North Atlantic, the opposite stochastic wind forcing generates the Atlantic meridional mode, which could decrease low clouds 316 over the South Atlantic (Tanimoto and Xie 2002) and Northeast Pacific (Miyamoto and Xie 2025). 317 These results indicate that extratropical stochastic atmospheric forcing triggers the subtropical lowcloud and meridional mode-like variability, thereby driving the GMTOA anomalies. This radiation 319 variability can be considered part of random radiative forcing for a simple stochastic model of the 320 global energy budget (Proistosescu et al. 2018). 321

In summary, decadal TOA radiation changes are dominated by subtropical low cloud decks, without prominent concurrent SST anomalies in the deep tropics. Extratropical stochastic variability
makes a pronounced contribution to generating subtropical SST and low cloud anomalies. These
SST anomalies, in turn, enable the AMIP to capture changes in GMTOA through low cloud-SST
feedback. The dominance of the subtropical SST effect contrasts sharply with the interannual
GMTOA variations.

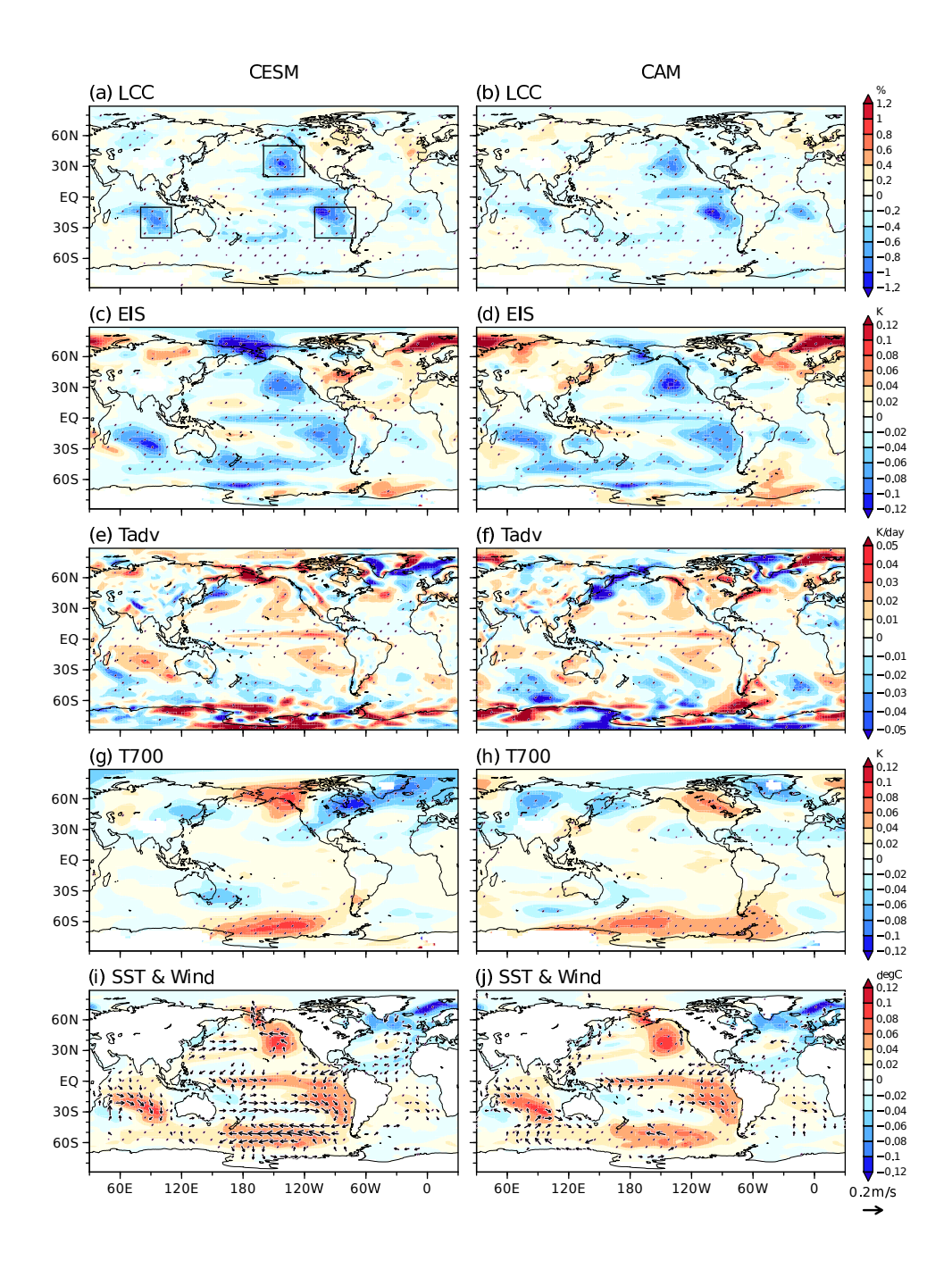


Fig. 7. As in Fig. 4, but for CESM decadal anomalies at lag +1 year. Black boxes in (a) indicate averaging domains for Table 2.

Table 2. Lag +1-year area-average surface heat fluxes (Q_{net} =LH_a+LH_o+SH+SW+LW) regressed onto decadal GMTOA variability in CESM. Unit is W m⁻² (positive values for downward flux). The averaging domains are shown in Fig. 7a. See Appendix for the latent heat flux decomposition.

	LHa	SH	SW+LW	Q _{net}
North Pacific	0.17	0.03	0.41	0.32
South Indian Ocean	0.38	0.04	0.49	0.53
South Pacific	0.39	0.06	0.43	0.5

5. Discussion

357

a. Comparison with CERES observations 334

Although short, the CERES observations serve as a valuable testbed to corroborate the findings 335 from CESM. Here, we analyze 21-year (2001-2021) detrended anomalies of GMTOA in the CERES observations and two AMIP simulations (CAMobs and AMobs). We perform ensemble averaging 337 of the AMIP results prior to analysis. 338

Despite the weaker lagged correlation with GMST, the observed lead-lag relationship of GMTOA 339 and GMST is out-of-phase (Figs. 2k,l), aligned with the CESM result. Around the GMTOA peak, 340 CRE dominates the GMTOA anomalies while the clear-sky effect is secondary (Figs. 2m,n and 341 Table 1). Although the reproducibility of AMIPs can be degraded by not only stochastic noise but also model biases, the two AMIPs reproduce the observed GMTOA and CRE reasonably well 343 (Figs. 2k,m), indicative of the SST effect. 344

The corresponding patterns of net radiation in the observations and AMIP simulations are shown 345 in Figs. 8a-c. Both the observations and AMIPs feature increased incoming radiation over the equatorial eastern Pacific and subtropical Southeast Pacific accompanied by decrease in low clouds 347 (Figs. 8d-f). Consistent with the emergence of ENSO discussed previously, positive SST anomalies 348 appear along the equatorial Pacific (Fig. 8g) in the phase transition from La Niña to El Niño (Fig. 349 20) accompanied by anomalous warm advection (Figs. S7d-f) and decreased EIS (Figs. S7a-c). 350 Cooling in tropical tropospheric temperature is somehow inconsistent between observations and 351 AMIPs (Figs. S7g-i), and its effect on GMTOA is unclear. The weaker relationship with ENSO in observations may reflect the short observational record, inclusion of decadal and forced changes, 353 and excessively strong ENSO in CESM (Capotondi et al. 2020). We note that extending the 354 CERES observations through 2024 to include the 2023-24 strong El Niño event (Xie et al. 2025; 355 Minobe et al. 2025; Peng et al. 2025) leads to a marginal increase in the maximum correlation 356 between GMTOA and Niño-3.4 SST, from 0.4 to 0.5.

Positive TOA radiation anomalies over the subtropical Southeast Pacific correspond to a local 358 rise in SST (Fig. 8g), suggestive of low cloud-SST feedback that is responsible for the AMIP reproducibility. The low cloud-SST co-variations are triggered by anomalous northwesterlies associated 360 with extratropical cyclonic circulations (Fig. 8g). The AMIP simulations fail to reproduce the circulation pattern (Figs. 8h,i), indicating the predominance of stochastic atmospheric variability.

Similar stochastically forced low cloud-SST feedback is found in the CESM interannual variations,

where local maxima in net radiation and low cloud decrease over the Southeast Pacific (Figs. 3c

and 4a) are accompanied by anomalous northwesterlies that are underestimated in CAM (Figs.

4i,j).

In summary, the CERES observations provide support for the contribution of ENSO and subtropical low cloud-SST feedback to GMTOA variations identified in CESM. A longer record is necessary to enhance the signal-to-noise ratio and isolate the decadal variability.

367

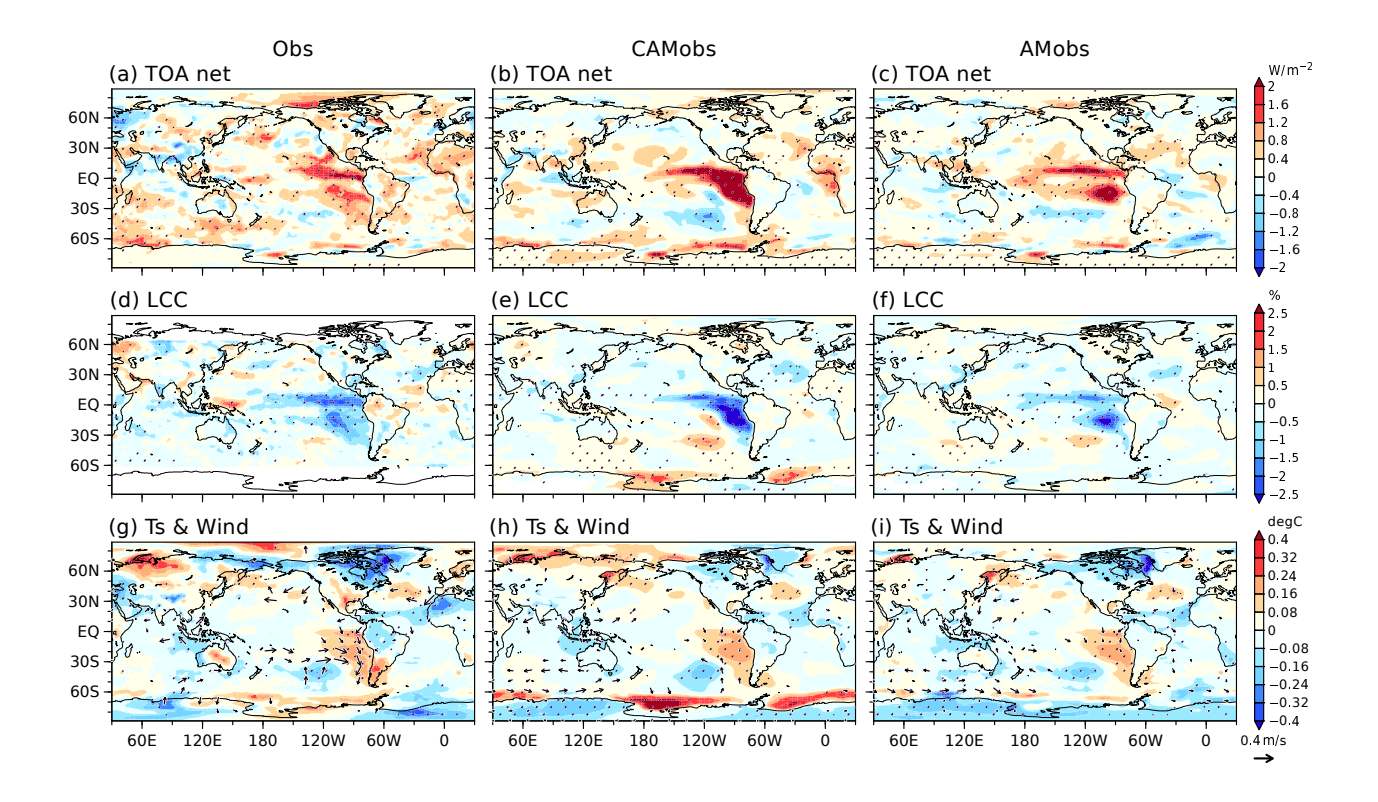


Fig. 8. Regression maps of (a,d,g) Observed, (b,e,h) CAMobs, and (c,f,i) AMobs anomalies onto CERES GMTOA at lag 0. (a-c) TOA radiation (W m⁻²). (d-f) Low cloud cover (%). (g-i) surface temperature (shading; °C) and wind (arrows; m s⁻¹; only points with the 90% confidence are drawn). Stippling indicates the 90% confidence.

b. Origin of timescale dependence

This study highlights two drivers of GMTOA variations via low cloud changes: ENSO and extratropical atmospheric variability. In CESM, the former dominates on interannual timescales whereas the latter dominates on decadal timescales. It is not surprising that ENSO, the strongest natural mode of variability, plays a major role in GMTOA fluctuations. ENSO is essentially an interannual oscillation arising from redistribution of tropical ocean heat content (Jin 1997), with a period of 2-8 years in both observations and CESM2 (Capotondi et al. 2020). Meanwhile, SST variations driven by extratropical atmospheric forcing become more important on decadal and longer timescales through stochastic reddening (Hasselmann 1976). This diminishes the relative importance of equatorial Pacific-forced GMTOA variability on decadal timescales.

Still, TPDV has statistically significant lagged correlations with GMTOA (Figs. 2e and 6). In 384 addition to forcing GMTOA, TPDV may be driven in part by extratropical atmospheric variability. 385 Previous studies argued that subtropical Northeast and Southeast Pacific SST anomalies forced by atmospheric stochastic variability can modulate TPDV via Pacific meridional modes (Vimont 387 2005; Okumura 2013; Di Lorenzo et al. 2015; Sun and Okumura 2019). Indeed, such meridional 388 mode-like patterns are found in the Pacific after the GMTOA peak (Figs. 6f,h,j). The induced TPDV may help shape the coherent pattern of CRE anomalies of the same sign in subtropical low 390 cloud decks through teleconnections. Further studies—say by using partially coupled runs—are 391 needed to better understand the cause and effect of low cloud variability, particularly the relative contributions of tropical and extratropical forcings. 393

6. Conclusion

This study investigates the natural variability of GMTOA based on a 500-year CESM2 preindustrial simulation and a corresponding perfect-model AMIP simulation. We show that the low-cloud
radiative effect plays a dominant role in the GMTOA variations, with spatial patterns that differ
markedly between interannual and decadal timescales. This difference reflects the relative influence of two distinct drivers: equatorial Pacific variability (e.g., ENSO) on interannual timescales
and extratropical atmospheric variability on decadal timescales. The CERES observations hint at
the influence of both drivers on GMTOA.

On interannual timescales, low cloud anomalies are distributed across tropical and extratropical 402 oceans, with maxima over the equatorial eastern Pacific in the transition phase of ENSO. During 403 positive GMTOA anomalies, reduced low cloud cover over the northeastern equatorial Pacific 404 arises from anomalous warm advection due to a developing El Niño. Meanwhile, the remaining broad decrease in low clouds aligns with weakened stability primarily during the decaying phase 406 of La Niña, which leaves an imprint on free-troposphere temperature and SST nonlocally through 407 teleconnections. In contrast, decadal GMTOA variability features more localized radiation anomalies in the eastern subtropical low cloud decks without concurrent SST changes in the deep tropics. These cloud anomalies are collocated with underlying SST anomalies, which allow AMIPs to 410 reproduce the CRE changes through low cloud-SST feedback. The low cloud-SST co-variations 411 are triggered by stochastic wind anomalies associated with extratropical atmospheric variability. 412 This timescale dependence likely reflects the nature of these drivers: ENSO peaks on interan-413 nual timescales due to tropical ocean dynamics, while extratropical forcing becomes increasingly 414 important on longer timescales. This study for the first time emphasizes the importance of the extratropical-forced subtropical low cloud-SST variations on GMTOA. 416

This study demonstrates the importance of SST patterns for GMTOA through a perfect model framework. In the unforced pattern effect, low cloud anomalies are driven not only by equatorial Pacific SST but also by stochastically forced eastern subtropical SST. As ENSO and TPDV can also drive the low cloud-SST variations (Yang et al. 2023), it remains challenging to assess their relative contributions only by using AMIP simulations forced with regional SST anomalies, e.g., the Green's function approach (Zhou et al. 2017; Bloch-Johnson et al. 2024). To address this, ocean-atmosphere coupled modeling or advanced statistical techniques are likely to be required.

We find that the spatial pattern of TOA radiation anomalies associated with GMTOA variability markedly differs from that associated with GMST variability, which is characterized by pronounced signals in the equatorial Pacific and high latitudes (Kosaka and Xie 2013; Xie et al. 2016; Deser et al. 2017). This discrepancy implies a redistribution of heat by atmospheric and oceanic circulations. The energy input may not only be passively advected but interact with the circulations. One plausible mechanism inferred from the decadal variations is that anomalous heat uptake in the North and South Pacific may propagate equatorward via the joint low cloud-WES feedback (Bellomo et al. 2014; Kim et al. 2022; Miyamoto et al. 2023) and subsurface ocean adjustment

(Luongo et al. 2025), potentially modulating TPDV and consequently GMST. The role of coupled dynamics in linking global energy imbalance to temperature patterns warrants further investigation.

CERES data reveal a marked positive trend of GMTOA over the past two decades. The associated SST warming is pronounced in the Northeast Pacific, the South Indian Ocean, and the South Atlantic (Fig. 4 in Loeb et al. 2024). This pattern bears some resemblance to that of the unforced GMTOA variations identified in this study. Given the importance of subtropical low clouds in both forced and unforced GMTOA variability, it is essential to carefully attribute the observed changes.

Although partially supported by the observational datasets, this study is primarily based on a 439 single model and subject to model biases, including excessively strong ENSO in CESM2 (discussed 440 in Section 5). In addition to the bias in equatorial Pacific variability, Tsuchida et al. (2023) 441 suggested that the sensitivity of tropical atmosphere to anomalous equatorial SST also contributes 442 to the intermodel spread in GMTOA variations. Moreover, many climate models underestimate 443 subtropical low cloud-SST feedback (Kim et al. 2022; Kang et al. 2023), which is, however, 444 strong in CESM2 (Kang et al. 2023; Larson et al. 2024; Miyamoto and Xie 2025). As low clouds are a critical factor in the uncertainty of climate feedback (Zelinka et al. 2020), natural 446 GMTOA variations may be related to the spread of projected warming (Zhou et al. 2015; Lutsko and 447 Takahashi 2018). Improvements of these biases promise a unified understanding of natural GMTOA 448 variability in a multi-model framework. Together with a better understanding of radiatively forced 449 response, this will ultimately help us understand the historical GMTOA variations and constrain 450 future projections.

Acknowledgments. We thank Prof. Dan Vimont and two anonymous reviewers for their constructive comments that greatly improved the manuscript. We thank Dr. Isla Simpson for setting up the perfect-model CAM6 simulation and CESM CVCWG for making CESM2/CAM6 simulations publicly available. A.M. and S.-P.X. were supported by the National Science Foundation (NSF, AGS 2105654). The Japanese Ministry of Education, Culture, Sports, Science and Technology (MEXT) program for the advanced studies of climate change projection (JPMXD0722680395) provided the computational resources for the AM4 simulation. The National Center for Atmospheric Research (NCAR) is sponsored by the NSF under Cooperative Agreement 1852977.

Data availability statement. The observational data used in this study are available online (ERA5: https://cds.climate.copernicus.eu; CERES-EBAF: https://ceres.larc.nasa.gov/data; MODIS: https://ladsweb.modaps.eosdis.nasa.gov/archive/allData/61/MOD08_D3; OISST: https://psl.noaa.gov/data/gridded/data.noaa.oisst.v2.highres.html). CESM2 and CAM6 simulations were downloaded from the casper system in National Center for Atmospheric Research. The authors can provide AM4 experiments upon reasonable requests.

7 APPENDIX

468

Decomposition of surface heat flux

Anomalous surface heat flux can be decomposed into latent heat (LH), sensible heat (SH), shortwave (SW), and longwave (LW) components. LH is a mixture of atmosphere-driven and SST-damping components. Following Xie et al. (2010), the SST damping term may be cast as

$$LH'_{o} = \overline{LH} \left(\frac{1}{\overline{q_s}} \frac{d\overline{q_s}}{dT_a} \right) SST'$$
(A1)

where T_a and q_s are air temperature and saturation specific humidity following the ClausiusClapeyron equation, respectively. Overbar and prime denote monthly climatology and anomaly,
respectively. The residual of anomalous latent heat flux represents the atmosphere-driven component (LH'_a) related to anomalous atmospheric conditions,

$$LH'_{a} = LH' - LH'_{o}. \tag{A2}$$

476 References

- Alexander, M. A., I. Bladé, M. Newman, J. R. Lanzante, N.-C. Lau, and J. D. Scott, 2002: The
- atmospheric bridge: The influence of ENSO teleconnections on air-sea interaction over the
- global oceans. J. Climate, 15, 2205–2231, https://doi.org/10.1175/1520-0442(2002)015(2205:
- 480 TABTIO ≥ 2.0.CO; 2.
- Andrews, T., and Coauthors, 2022: On the effect of historical SST patterns on radiative feedback.
- J. Geophys. Res., **127**, e2022JD036675, https://doi.org/10.1029/2022JD036675.
- Andrews, T., and M. J. Webb, 2018: The dependence of global cloud and lapse rate feedbacks
- on the spatial structure of tropical Pacific warming. J. Climate, 31, 641–654, https://doi.org/
- 10.1175/JCLI-D-17-0087.1.
- Andrews, T., and Coauthors, 2018: Accounting for changing temperature patterns increases his-
- torical estimates of climate sensitivity. Geophys. Res. Lett., 45, 8490–8499, https://doi.org/
- 488 10.1029/2018GL078887.
- Bellomo, K., A. Clement, T. Mauritsen, and B. Stevens, 2014: Simulating the role of subtrop-
- ical stratocumulus clouds in driving Pacific climate variability. J. Climate, 27, 5119–5131,
- https://doi.org/10.1175/JCLI-D-13-00548.1.
- Bloch-Johnson, J., and Coauthors, 2024: The Green's function model intercomparison project
- (GFMIP) protocol. J. Adv. Model. Earth Syst., 16, e2023MS003700, https://doi.org/10.1029/
- ⁴⁹⁴ 2023MS003700.
- ⁴⁹⁵ Capotondi, A., C. Deser, A. S. Phillips, Y. M. Okumura, and S. M. Larson, 2020: ENSO and
- Pacific Decadal Variability in the Community Earth System Model version 2. J. Adv. Model.
- Earth Syst., **12**, e2019MS002022, https://doi.org/10.1029/2019MS002022.
- ⁴⁹⁸ Ceppi, P., and S. Fueglistaler, 2021: The El Niño-Southern Oscillation pattern effect. *Geophys*.
- Res. Lett., 48, e2021GL095261, https://doi.org/10.1029/2021GL095261.
- 500 Chiang, J. C. H., and D. J. Vimont, 2004: Analogous Pacific and Atlantic meridional modes
- of tropical atmosphere-ocean variability. J. Climate, 17, 4143–4158, https://doi.org/10.1175/
- 502 JCLI4953.1.

- Danabasoglu, G., and Coauthors, 2020: The community earth system model version 2 (CESM2).
- J. Adv. Model. Earth Syst., 12, e2019MS001916, https://doi.org/10.1029/2019MS001916.
- Deser, C., R. Guo, and F. Lehner, 2017: The relative contributions of tropical Pacific sea surface
- temperatures and atmospheric internal variability to the recent global warming hiatus. *Geophys*.
- Res. Lett., 44, 7945–7954, https://doi.org/10.1002/2017GL074273.
- Deser, C., and J. M. Wallace, 1990: Large-scale atmospheric circulation features of warm
- and cold episodes in the tropical Pacific. J. Climate, 3, 1254–1281, https://doi.org/10.1175/
- 1520-0442(1990)003(1254:LSACFO)2.0.CO;2.
- Dessler, A. E., T. Mauritsen, and B. Stevens, 2018: The influence of internal variability on Earth's
- energy balance framework and implications for estimating climate sensitivity. *Atmos. Chem.*
- Phys., **18**, 5147–5155, https://doi.org/10.5194/acp-18-5147-2018.
- Di Lorenzo, E., G. Liguori, N. Schneider, J. C. Furtado, B. T. Anderson, and M. A. Alexander,
- 2015: ENSO and meridional modes: A null hypothesis for Pacific climate variability. *Geophys*.
- Res. Lett., **42**, 9440–9448, https://doi.org/10.1002/2015GL066281.
- Dong, Y., K. C. Armour, M. D. Zelinka, C. Proistosescu, D. S. Battisti, C. Zhou, and T. Andrews,
- 2020: Inter-model spread in the sea-surface temperature pattern effect and its contribution to
- climate sensitivity in CMIP5 and CMIP6 models. J. Climate, 33, 7755–7775, https://doi.org/
- 10.1175/JCLI-D-19-1011.1.
- Enfield, D. B., and D. A. Mayer, 1997: Tropical Atlantic sea surface temperature variability and
- its relation to El Niño-Southern Oscillation. J. Geophys. Res., 102, 929–945, https://doi.org/
- 10.1029/96JC03296.
- Evan, A. T., R. Allen, R. Bennartz, and D. J. Vimont, 2013: The modification of sea surface
- temperature anomaly linear damping time scales by stratocumulus clouds. J. Climate, 26, 3619–
- 3630, https://doi.org/10.1175/JCLI-D-12-00370.1.
- Eyring, V., S. Bony, G. A. Meehl, C. A. Senior, B. Stevens, R. J. Stouffer, and K. E. Taylor,
- 2016: Overview of the Coupled Model Intercomparison Project phase 6 (CMIP6) experimental
- design and organization. Geoscientific Model Development, 9, 1937–1958, https://doi.org/10.
- 5194/gmd-9-1937-2016.

- Fueglistaler, S., 2019: Observational evidence for two modes of coupling between sea surface temperatures, tropospheric temperature profile, and shortwave cloud radiative effect in the
- tropics. *Geophys. Res. Lett.*, **46**, 9890–9898, https://doi.org/10.1029/2019GL083990.
- Gregory, J., and Coauthors, 2004: A new method for diagnosing radiative forcing and climate sensitivity. *Geophys. Res. Lett.*, **31**, L03205, https://doi.org/10.1029/2003GL018747.
- Gregory, J. M., and T. Andrews, 2016: Variation in climate sensitivity and feedback parameters during the historical period. *Geophys. Res. Lett.*, **43**, 3911–3920, https://doi.org/
- Hasselmann, K., 1976: Stochastic climate models Part I. Theory. *Tellus*, **28**, 473–485, https://doi.org/10.1111/j.2153-3490.1976.tb00696.x.
- Hersbach, H., and Coauthors, 2020: The ERA5 global reanalysis. *Quart. J. Roy. Meteor. Soc.*, **146**,
 1999–2049, https://doi.org/10.1002/qj.3803.
- Huang, B., P. W. Thorne, V. F. Banzon, T. Boyer, G. Chepurin, and J. H. Lawrimore, 2017:
 Extended reconstructed sea surface temperature, version 5 (ERSSTv5): Upgrades, validations,
 and intercomparisons. J. Climate, 30, 8179–8205, https://doi.org/10.1175/JCLI-D-16-0836.1.
- Jin, F.-F., 1997: An equatorial ocean recharge paradigm for ENSO. Part 1: Conceptual model.

 J. Atmos. Sci., **54**, 811–829, https://doi.org/10.1175/1520-0469(1997)054\(0811:AEORPF\)2.0.

 CO;2.
- Kang, S. M., P. Ceppi, Y. Yu, and I.-S. Kang, 2023: Recent global climate feedback controlled by Southern Ocean cooling. *Nat. Geosci.*, **16**, 775–780, https://doi.org/10.1038/s41561-023-01256-6.
- Kim, H., S. M. Kang, J. E. Kay, and S.-P. Xie, 2022: Subtropical clouds key to Southern
 Ocean teleconnections to the tropical Pacific. *Proc. Natl. Acad. Sci. (USA)*, **119**, e2200514119,
 https://doi.org/10.1073/pnas.2200514119.
- Klein, S. A., and D. L. Hartmann, 1993: The seasonal cycle of low stratiform clouds. *J. Climate*,
 6, 1587–1606, https://doi.org/10.1175/1520-0442(1993)006(1587:TSCOLS)2.0.CO;2.

- Kosaka, Y., and S.-P. Xie, 2013: Recent global-warming hiatus tied to equatorial Pacific surface cooling. *Nature*, **501**, 403–407, https://doi.org/10.1038/nature12534.
- Larson, S. M., K. McMonigal, Y. Okumura, D. Amaya, A. Capotondi, K. Bellomo, I. R.
- Simpson, and A. C. Clement, 2024: Ocean complexity shapes sea surface temperature vari-
- ability in a CESM2 coupled model hierarchy. J. Climate, 37, 4931–4948, https://doi.org/
- 10.1175/JCLI-D-23-0621.1.
- Loeb, N. G., S.-H. Ham, R. P. Allan, T. J. Thorsen, B. Meyssignac, S. Kato, G. C. Johnson, and
- J. M. Lyman, 2024: Observational assessment of changes in Earth's energy imbalance since
- ⁵⁶⁵ 2000. Surv. Geophys., **45**, 1757–1783, https://doi.org/10.1007/s10712-024-09838-8.
- Loeb, N. G., and Coauthors, 2018: Clouds and the Earth's Radiant Energy System (CERES)
- Energy Balanced and Filled (EBAF) Top-of-Atmosphere (TOA) Edition-4.0 data product. J.
- ⁵⁶⁸ Climate, **31**, 895–918, https://doi.org/10.1175/JCLI-D-17-0208.1.
- Luongo, M. T., S.-P. Xie, I. Eisenman, S. Sun, and Q. Peng, 2025: How the subsurface tropical
- Pacific responds to subtropical surface cooling: Implications for cross-equatorial transport. J.
- *Climate*, **38**, 3313–3331, https://doi.org/10.1175/JCLI-D-24-0440.1.
- Lutsko, N. J., and K. Takahashi, 2018: What can the internal variability of CMIP5 models
- tell us about their climate sensitivity? J. Climate, 31, 5051–5069, https://doi.org/10.1175/
- JCLI-D-17-0736.1.
- Metz, W., 1991: Optimal relationship of large-scale flow patterns and the barotropic feedback due to
- high-frequency eddies. J. Atmos. Sci., 48, 1141–1159, https://doi.org/10.1175/1520-0469(1991)
- 048(1141:OROLSF)2.0.CO;2.
- Minobe, S., E. Behrens, K. L. Findell, N. G. Loeb, B. Meyssignac, and R. Sutton, 2025: Global
- and regional drivers for exceptional climate extremes in 2023-2024: beyond the new normal.
- npj Clim. Atmos. Sci., **8**, 138, https://doi.org/10.1038/s41612-025-00996-z.
- Miyamoto, A., H. Nakamura, and T. Miyasaka, 2018: Influence of the subtropical high and storm
- track on low-cloud fraction and its seasonality over the south Indian Ocean. J. Climate, 31,
- ⁵⁸³ 4017–4039, https://doi.org/10.1175/JCLI-D-17-0229.1.

- Miyamoto, A., H. Nakamura, S.-P. Xie, T. Miyasaka, and Y. Kosaka, 2023: Radiative impacts of
- Californian marine low clouds on North Pacific climate in a global climate model. J. Climate,
- 36, 8443–8459, https://doi.org/10.1175/JCLI-D-23-0153.1.
- Miyamoto, A., and S.-P. Xie, 2025: Low cloud-SST variability over the summertime subtrop-
- ical northeast Pacific: Role of extratropical atmospheric modes. J. Climate, 38, 165–180,
- https://doi.org/10.1175/JCLI-D-24-0015.1.
- Okumura, Y. M., 2013: Origins of tropical Pacific decadal variability: Role of stochas-
- tic atmospheric forcing from the South Pacific. J. Climate, 26, 9791–9796, https://doi.org/
- ⁵⁹² 10.1175/JCLI-D-13-00448.1.
- Olonscheck, D., and M. Rugenstein, 2024: Coupled climate models systematically underestimate
- radiation response to surface warming. *Geophys. Res. Lett.*, **51**, e2023GL106909, https://doi.org/
- 10.1029/2023GL106909.
- Peng, Q., S.-P. Xie, A. Miyamoto, C. Deser, P. Zhang, and M. T. Luongo, 2025: Strong 2023-
- ⁵⁹⁷ 24 El Niño generated by ocean dynamics. *Nat. Geosci.*, **18**, 471–478, https://doi.org/10.1038/
- s41561-025-01700-9.
- Platnick, S., M. D. King, S. A. Ackerman, W. P. Menzel, B. A. Baum, J. C. Riedi, and R. A. Frey,
- 2003: The MODIS cloud products: Algorithms and examples from Terra. *IEEE Trans. Geosci.*
- Remote Sens., 41, 459–473, https://doi.org/10.1109/TGRS.2002.808301.
- Proistosescu, C., A. Donohoe, K. C. Armour, G. H. Roe, M. F. Stuecker, and C. M. Bitz, 2018:
- Radiative feedbacks from stochastic variability in surface temperature and radiative imbalance.
- 604 Geophys. Res. Lett., **45**, 5082–5094, https://doi.org/10.1029/2018GL077678.
- Raghuraman, S. P., D. Paynter, and V. Ramaswamy, 2021: Anthropogenic forcing and re-
- sponse yield observed positive trend in Earth's energy imbalance. *Nat. Commun.*, 12, 4577,
- https://doi.org/10.1038/s41467-021-24544-4.
- Rugenstein, M., M. Zelinka, K. B. Karnauskas, P. Ceppi, and T. Andrews, 2023: Patterns of surface
- warming matter for climate sensitivity. *Eos*, 104, https://doi.org/10.1029/2023EO230411.
- Senior, C. A., and J. F. B. Mitchell, 2000: The time-dependence of climate sensitivity. Geophys.
- Res. Lett., 27, 2685–2688, https://doi.org/10.1029/2000GL011373.

- Sherwood, S. C., and Coauthors, 2020: An assessment of Earth's climate sensitivity using multiple lines of evidence. *Rev. Geophys.*, **58**, e2019RG000678, https://doi.org/10.1029/2019RG000678.
- Small, R. J., S.-P. Xie, Y. Wang, S. K. Esbensen, and D. Vickers, 2005: Numerical simulation of boundary layer structure and cross-equatorial flow in the eastern Pacific. *J. Atmos. Sci.*, **62**, 1812–1830, https://doi.org/10.1175/JAS3433.1.
- Sobel, A. H., J. Nilsson, and L. M. Polvani, 2001: The weak temperature gradient approximation and balanced tropical moisture waves. *J. Atmos. Sci.*, **58**, 3650–3665, https://doi.org/10.1175/1520-0469(2001)058(3650:TWTGAA)2.0.CO;2.
- Sun, T., and Y. M. Okumura, 2019: Role of stochastic atmospheric forcing from the South and
 North Pacific in tropical Pacific decadal variability. *J. Climate*, **32**, 4013–4038, https://doi.org/
 10.1175/JCLI-D-18-0536.1.
- Tanimoto, Y., and S.-P. Xie, 2002: Inter-hemispheric decadal variations in SST, surface wind, heat flux and cloud cover over the Atlantic ocean. *J. Meteor. Soc. Japan*, **80**, 1199–1219.
- Tsuchida, K., T. Mochizuki, R. Kawamura, T. Kawano, and Y. Kamae, 2023: Diversity of lagged relationships in global means of surface temperatures and radiative budgets for CMIP6 piControl simulations. *J. Climate*, **36**, 8743–8759, https://doi.org/10.1175/JCLI-D-23-0045.1.
- Vimont, D. J., 2005: The contribution of the interannual ENSO cycle to the spatial pattern of decadal ENSO-like variability. *J. Climate*, **18**, 2080–2092, https://doi.org/10.1175/JCLI3365.1.
- Wills, R. C. J., K. C. Armour, D. S. Battisti, C. Proistosescu, and L. A. Parsons, 2021: Slow modes
 of global temperature variability and their impact on climate sensitivity estimates. *J. Climate*,
 34, 8717–8738, https://doi.org/10.1175/JCLI-D-20-1013.1.
- Wood, R., and C. S. Bretherton, 2006: On the relationship between stratiform low cloud cover and lower-tropospheric stability. *J. Climate*, **19**, 6425–6432, https://doi.org/10.1175/JCLI3988.1.
- Xie, S.-P., C. Deser, G. A. Vecchi, J. Ma, H. Teng, and A. T. Wittenberg, 2010: Global warming pattern formation: Sea surface temperature and rainfall. *J. Climate*, **23**, 966–986, https://doi.org/

- Xie, S.-P., K. Hu, J. Hafner, H. Tokinaga, Y. Du, G. Huang, and T. Sampe, 2009: Indian Ocean capacitor effect on Indo-Western Pacific climate during the summer following El Niño. *J. Climate*, 22, 730–747, https://doi.org/10.1175/2008JCLI2544.1.
- Xie, S.-P., Y. Kosaka, and Y. M. Okumura, 2016: Distinct energy budgets for anthropogenic and natural change during global warming hiatus. *Nat. Geosci.*, **9**, 29–33, https://doi.org/10.1038/ngeo2581.
- Xie, S.-P., A. Miyamoto, P. Zhang, Y. Kosaka, Y. Liang, and N. J. Lutsko, 2025: What made 2023 and 2024 the hottest years in a row? *npj Clim. Atmos. Sci.*, **8**, 117, https://doi.org/10.1038/s41612-025-01006-y.
- Xie, S.-P., and S. G. H. Philander, 1994: A coupled ocean-atmosphere model of relevance to the ITCZ in the eastern Pacific. *Tellus*, **46A**, 340–350, https://doi.org/10.3402/tellusa.v46i4.15484.
- Yang, L., S.-P. Xie, S. S. P. Shen, J.-W. Liu, and Y.-T. Hwang, 2023: Low cloud-SST feedback over the subtropical Northeast Pacific and the remote effect on ENSO variability. *J. Climate*, **36**, 441–452, https://doi.org/10.1175/JCLI-D-21-0902.1.
- Zelinka, M. D., T. A. Myers, D. T. McCoy, S. Po-Chedley, P. M. Caldwell, and P. Ceppi, 2020:
 Causes of higher climate sensitivity in CMIP6 models. *Geophys. Res. Lett.*, 47, e2019GL085782,
 https://doi.org/10.1002/2015GL067416.
- Zhang, H., A. Clement, and P. Di Nezio, 2014: The South Pacific meridional mode: A mechanism
 for ENSO-like variability. *J. Climate*, 27, 769–783, https://doi.org/10.1175/JCLI-D-13-00082.1.
- Zhao, M., and Coauthors, 2018: The GFDL global atmosphere and land model AM4.0/LM4.0:
 Simulation characteristics with prescribed SSTs. *J. Adv. Model. Earth Syst.*, 10, 691–734,
 https://doi.org/10.1002/2017MS001208.
- Zhou, C., M. D. Zelinka, A. E. Dessler, and S. A. Klein, 2015: The relationship between interannual
 and long-term cloud feedbacks. *Geophys. Res. Lett.*, 42, 10463–10469, https://doi.org/10.1002/
 2015GL066698.
- Zhou, C., M. D. Zelinka, and S. A. Klein, 2016: Impact of decadal cloud variations on the Earth's
 energy budget. *Nat. Geosci.*, 9, 871–874, https://doi.org/10.1038/ngeo2828.

- ⁶⁶⁵ Zhou, C., M. D. Zelinka, and S. A. Klein, 2017: Analyzing the dependence of global cloud feedback
- on the spatial pattern of sea surface temperature change with a Green's function approach. J.
- 667 Adv. Model. Earth Syst., 9, 2174–2189, https://doi.org/10.1002/2017MS001096.